Photoacoustics 42 (2025) 100692

Contents lists available at ScienceDirect

Photoacoustics

journal homepage: www.elsevier.com/locate/pacs

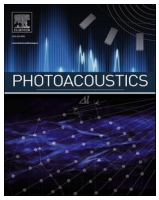

Multivariate-coupled-enhanced photoacoustic spectroscopy with Chebyshev rational fractional-order filtering algorithm for trace CH_4 detection

Shenlong Zha [a], Hang Chen [a], Chen Liu [a], Yuxiang Guo [a], Hongliang Ma [a], Qilei Zhang [a], Lingli Li [a], Shengbao Zhan [a], Gang Cheng [b], Yanan Cao [b], Pan Pan [a,*]

[a] School of Electronic Engineering and Intelligent Manufacturing, Anqing Normal University, Anqing, Anhui 246133, China
[b] State Key Laboratory of Mining Response and Disaster Prevention and Control in Deep Coal Mines, Anhui University of Science and Technology, Huainan 232001, China

ARTICLE INFO

Keywords:
Photoacoustic spectroscopy
Multivariate coupled amplification
Chebyshev rational fractional-order filtering
Detection limit
Measurement precision

ABSTRACT

An innovative and miniature photoacoustic spectroscopy (PAS) gas sensor based on a multivariate-coupled amplification photoacoustic cell (MVCA-PAC) with a total length of 100 mm was developed to achieve ultra-sensitive trace CH_4 detection. Acoustic pressure distribution simulations reveal that at the first-order resonance frequency, the MVCA-PAC achieves a maximum acoustic pressure approximately 3.9 times higher than that of a conventional photoacoustic cell. The absorption optical path of the MVCA-PAC reached 2068 mm through 22 reflections, resulting in a 2-fold increase in the amplitude of photoacoustic signals compared to the traditional photoacoustic cell with an equivalent absorption optical path. Furthermore, compared to a single-pass photoacoustic cell, the *2-f* signal intensity of the MVCA-PAC increased by a factor of 4.5. Allan variance analysis indicated a detection limit of 0.572 ppm for CH_4 detection with an averaging time of approximately 300 s. To further improve the measurement precision of the designed sensor, the Chebyshev rational fractional-order filtering (CRFOF) algorithm was introduced for PAS signal processing for the first time. Post-processing results demonstrated a 15.4-fold improvement in measurement precision, achieving a precision of 0.578 ppm. Finally, continuous monitoring of atmospheric CH_4 over a 48-hour period validated the reliability and feasibility of the sensor.

1. Introduction

Methane (CH_4) is a widely distributed energy gas in nature. It is both an essential element of natural gas and mine gas and a critical greenhouse gas that cannot be ignored[1–4]. Although methane is present in much lower concentrations in the atmosphere compared to carbon dioxide, its greenhouse effect is about 22 times more intense[5]. Human activities, including industrial production, livestock farming, sewage treatment, and energy extraction, are the primary contributors to the increasing methane concentration in the atmosphere. Therefore, monitoring trace methane concentration is critical for the precise control of methane emissions. Laser absorption spectroscopy, which operates based on Lambert-Beer's law, offers the advantages of high sensitivity, quick responsiveness, and excellent selectivity[6–14], making it a widely adopted method for trace gas detection in various applications such as atmospheric pollutant monitoring, industrial gas emission control, natural gas pipeline leak detection, agricultural ecology, and climate research[15–24]. Numerous methane gas sensors based on absorption spectroscopy, such as direct absorption spectroscopy (DAS), tunable diode laser absorption spectroscopy (TDLAS), photoacoustic spectroscopy (PAS) and cavity enhanced absorption spectroscopy technology (CEAS) have been developed[25,26]. Among these, PAS stands out due to its high sensitivity, large dynamic detection range and detector versatility. The minimum detection limit (MDL) and measurement precision are important parameters for evaluating the performance of PAS systems and researchers mainly focus on making efforts in terms of system structure optimization and signal-processing algorithm design [27–32]. The optimization of the PAS system structure involves selecting mid-infrared light sources, including quantum cascade lasers (QCL) and interband cascade lasers (ICL)[33–36], the utilization of novel

* Corresponding author.
E-mail address: panpan1988@semi.ac.cn (P. Pan).

https://doi.org/10.1016/j.pacs.2025.100692
Received 19 December 2024; Received in revised form 21 January 2025; Accepted 21 January 2025
Available online 31 January 2025

acoustic sensors and the innovative design of the photoacoustic cell structure. Benefit from the higher absorption coefficients of most gas molecules in the mid-infrared range，a multi-component PAS detection system based on an ICL light source emitted range from 3360 to 3372 nm was designed by Jonas Pangerl[37], detection limits of 6.8 ppbv, 2.3 ppbv, and 3.6 ppbv were achieved for CH_4, C_2H_6, and C_2H_2, respectively.

Up to now, excellent acoustic sensors such as MEMS microphone [38], Polyvinylidene Fluoride Film[39], quartz tuning forks[40–48] and cantilevers[49,50] have been used as alternatives to traditional electric microphones. For instance, Thomas Strahl et al.[51] developed a MEMS microphone based PAS sensor with a detection limit of 329 ppb for CH_4 detection. Similarly, Liu et al.[39] demonstrated a PAS sensor for H_2O vapor detection using a PVDF film as the transducer, achieving a minimum detection limit of 40 ppmv. Ma et al.[52] proposed a quartz-enhanced photoacoustic spectroscopy (QEPAS) sensor based on an H-shaped acoustic micro-resonator (AmR), which exhibited a 17.2-fold enhancement in sensitivity compared to a conventional QEPAS sensor using a bare quartz tuning fork (QTF) for water vapor detection.

The utilization of mid-infrared light sources and novel acoustic sensors has significantly enhanced the minimum detection limit of PAS systems, however, it still has imperfections. For instance, the high production costs of mid-infrared light sources, MEMS microphone, PVDF film and cantilever increase the overall cost of PAS sensors and impose stricter structural requirements. Additionally, the resonant frequencies of QTFs used in QEPAS systems generally exceeds 30 kHz, posing challenges for detecting molecules with low vibrational-translational (V-T) relaxation rates[53]. In contrast, enhancing the intensity of photoacoustic (PA) signals through the modification of PA cells is a more cost-effective and practical approach for improving the detection limit，so the Herriott-type and White-type multi-pass PA cells have been presented to address these challenges[54–56].

In terms of improving the measurement precision of PAS system, the design and application of appropriate filtering algorithms are often essential. Commonly used filtering algorithms include the multi-signal average filtering (MAF) algorithm, Savitzky-Golay (S-G) filtering algorithm, Kalman filtering algorithm, and wavelet denoising algorithm [57]. The MAF algorithm is simple and easy to implement, but is unsuitable for handling non-stationary or impulsive noise. The S-G filtering algorithm is effective at preserving the original shape and features of the signal while smoothing the data, however, it suffers from relatively high computational complexity, which can pose challenges in scenarios with large-scale datasets or stringent real-time requirements. The Kalman filtering algorithm is highly effective at managing system noise, but for non-linear systems, it requires necessary linearization approximation, which can introduce obvious deviations. The Wavelet denoising algorithm, with its ability to perform multi-resolution analysis, effectively separates signals and noise based on their characteristics at different scales. Nevertheless, the selection of wavelet basis functions will influence the denoising effect, and selecting appropriate wavelet basis functions is rather complicated.

To improve the detection performance of the miniaturized PAS sensor, we propose a multivariate coupling amplification approach for PAS signals by integrating multi-pass optical paths and T-shaped acoustic waveguide. Furthermore, the Chebyshev rational fractional-order filtering (CRFOF) algorithm was introduced into the signal processing workflow for the first time. This algorithm effectively addresses the limitations of conventional filtering algorithms while enhancing measurement precision. The performance of the MVCA-PAC and the effectiveness of the CRFOF filtering algorithm were evaluated through the detection of CH_4 gas. Additionally, the system successfully achieved accurate online monitoring of atmospheric methane concentrations over a 48-hour period, demonstrating its reliability and practicality.

2. Model of Chebyshev rational fractional-order filtering algorithm

The Chebyshev filtering algorithm based on fractional-order rational functions provides continuous stepwise stopband attenuation rates and enhanced design flexibility. This approach enables effective preservation of the spectral characteristics of PAS signals, making it well-suited for advanced signal processing applications. The transfer function is expressed as:

$$H\left(j\omega\right) = \frac{c}{(j\omega)^{1+\alpha} + a(j\omega)^{\alpha} + b} \tag{1}$$

Whereα, a, b, and c are parameters that need to be optimized. Assuming the input PAS signal is $S_{PA\text{-}in}$, the output signal is given by:

$$S_{PA-out} = H(j\omega)S_{PA-in} \tag{2}$$

When the frequencyωapproaches zero, $H(j\omega)$approaches $\frac{c}{b}$, the output signal is $S_{PA-out} = \frac{c}{b}S_{PA-in}$, indicating that low-frequency signals are preserved. When the ωapproaches infinity, $H(j\omega)$approaches 0, $S_{PA-out} = 0$, meaning that high-frequency signals are filtered out.

The calculation formulas for the order (N) and ripple coefficient (ε) of a Chebyshev filter are expressed as follows:

$$N = \frac{\cosh^{-1}\left[\frac{\sqrt{\delta_s^{-2}-1}}{\sqrt{\left(1-\delta_p\right)^{-2}-1}}\right]}{\cosh^{-1}\left(\frac{\omega_s}{\omega_p}\right)} \tag{3}$$

$$\varepsilon = \sqrt{\left(1-\delta_p\right)^{-2}-1} \tag{4}$$

Where δ_p, δ_s, ω_p, and ω_s denote the passband deviation, stopband deviation, passband edge frequency, and stopband edge frequency, respectively. Their relationship is defined as follows:

$$\left|H(j\omega_p)\right| \geq 1-\delta_p \left|H(j\omega_s)\right| \leq \delta_s \tag{5}$$

The amplitude-frequency response of the normalized Chebyshev low-pass filter is defined as:

$$\left|C_{n+\alpha}(\omega_i)\right| = \frac{1}{\sqrt{1+\varepsilon^2 T_{n+\alpha}^2(\omega_i)}}, \qquad \left(n = N-\alpha\right) \tag{6}$$

$T_{n+\alpha}$represents the fractional-order Chebyshev polynomial, and its expression is given as follows:

$$T_{n+\alpha}(\omega) = \begin{cases} \cos((n+\alpha) * \arccos(\omega)), |\omega| \leq 1 \\ \cosh((n+\alpha) * \arccosh(\omega)), |\omega| > 1 \end{cases} \tag{7}$$

Define the nonlinear least squares cost function as: $\frac{1}{2}\sum_{i=1}^{K}\left(\left|H_{n+\alpha}(\mathrm{X},\omega_i) - C_{n+\alpha}(\omega_i)\right|\right)^2$, where X is a vector composed of four parameters: α, a, b, and c. The cost function is expanded using a Taylor series at $X^* = X + \Delta X$, and the point where its first derivative equals zero is calculated. This point is then substituted into the cost function to evaluate whether its second derivative is positive definite. When the second derivative is positive definite, the point is substituted into Eq. (1) to calculate the output signal. If it is not positive definite, the passband deviation and stopband deviation are iteratively adjusted until the second derivative becomes positive definite. The comprehensive implementation process is illustrated in Fig. 1.

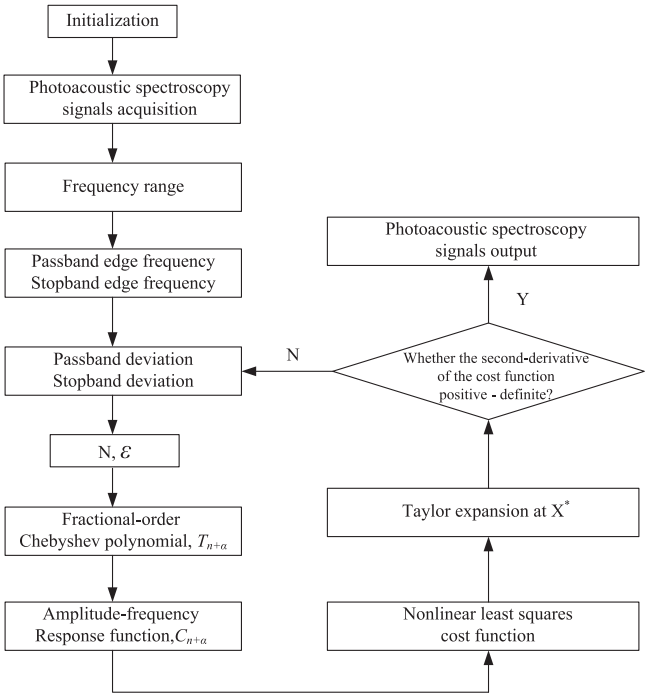

Fig. 1. Flow chart of Chebyshev rational fractional-order filtering algorithm.

3. Experiment details

3.1. Multivariate coupled amplification PA cell (MVCA-PAC) configuration

The structure of the multivariate coupled amplification PA cell is shown in Fig. 2. It comprises of a cylindrical resonator, two buffer cavities and T-shaped acoustic waveguide. The resonator measures 60 mm in length and 5 mm in diameter. To suppress ambient noise, a pair of buffer cavities, each 17 mm long and 20 mm in diameter, are placed at its ends. The total length of the T-shaped acoustic waveguide is 10 mm. The front-stage and rear-stage waveguides are 8 mm and 2 mm in length, respectively, with diameters of 1 mm and 5 mm, respectively. Two spherical reflectors, each with a diameter of 25 mm, are placed parallel to each other and are separated by 176 mm at both ends of the buffer cavities. The incident light enters the resonant cavity through a fiber optic collimator at a specific angle. The optical path of the multiple reflections between the two spherical mirrors was simulated by TracePro software. The ray tracing model is illustrated in Fig. 3, and the schematic and experimentally observed light spot distributions are shown in Fig. 4(a) and (b), respectively. It is obvious that the light spots on the reflective mirrors form a circular pattern with a diameter of

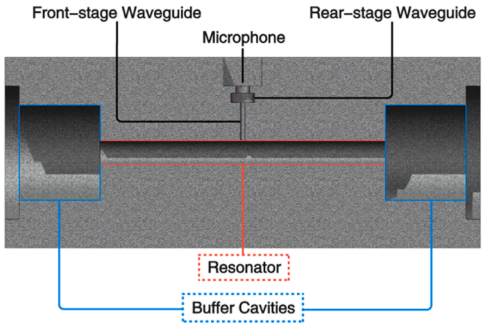

Fig. 2. Structure of the multivariate coupled amplification PA cell with a cylindrical resonant cavity and a T-shaped acoustic waveguide.

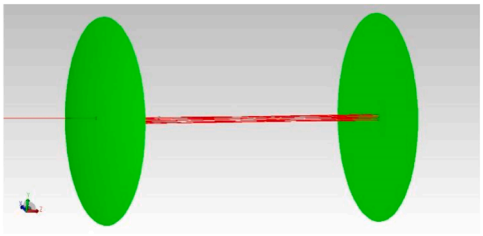

Fig. 3. Schematic diagram of the optical path of MVCA-PAC.

approximately 4 mm, which is smaller than the diameter of the resonant cavity. This design effectively prevents the modulated light from being absorbed by the sidewall. Considering the spacing and spot distribution of the spherical mirrors, the total absorption path length was calculated to be approximately 2068 mm. Multiple reflections significantly increase the absorption of the modulated light by the molecules to be measured. Acoustic standing waves are generated in the resonant cavity through non-radiative relaxation. When the modulation frequency of the incident light matches the first-order resonance frequency of the MVCA-PAC, the occurrence of resonance leads to a substantial enhancement of the acoustic wave amplitude. Simulations in COMSOL Multiphysics were performed to evaluate the distribution of acoustic pressure and the frequency characteristics of the PA cell. Fig. 5(a) and (b) compare the acoustic pressure distributions of the MVCA-PAC and a traditional resonant PA cell with buffer and resonance cavities of the same size. In the traditional resonant PA cell, the maximum acoustic pressure is concentrated at the middle of the resonant cavity, whereas in the MVCA-PAC, the peak acoustic pressure occurs at the end of the rear-stage waveguide. The simulated acoustic pressure amplitude-frequency response curves of the MVCA-PAC and the traditional resonant PA cell are shown in Fig. 6(a) and (b), respectively. The first-order resonant frequency of the MVCA-PAC was approximately 3058 Hz, with its peak acoustic pressure being 3.9 times higher than that of the traditional PA cell, which had a first-order resonance frequency of 2827 Hz.

3.2. Experimental setup

The schematic diagram of the MVCA-PAC based PAS sensor setup is shown in Fig. 7. A near-infrared DFB semiconductor laser with an emission wavelength of 1653 nm was employed as the excitation light source. The modulation of the DFB laser was realized by combining a triangular wave with a frequency of 1 Hz and an amplitude of 650 mV from the RIGOL DG4062 function generator with a sine wave generated by the Stanford Research Systems SR830 lock-in amplifier. The modulated laser light was coupled into the MVCA-PAC through a collimator. Within the resonant cavity, the light underwent multiple reflections, effectively increasing the optical absorption path for CH_4 gas. The PAS signal generated within the resonator was detected using a high-sensitivity microphone installed at the end of the rear-stage acoustic waveguide. The PAS signal captured by the microphone was first processed through a pre-amplifier (Stanford Research Systems, SR650) for amplification, followed by demodulation at the modulation frequency with a lock-in amplifier to obtain the second harmonic (*2-f*) signal. The amplification factor of the pre-amplifier is set to 10 dB and the lock-in amplifier has a time constant of 10 ms. The processed signal was acquired using a National Instruments USB-6356 data acquisition card and visualized on a PC through an interface developed in LabVIEW.

4. Results and discussion

4.1. Resonance frequency analysis

The determination of the resonance frequency of the PA cell is critical for generating the strongest PAS signal. To ensure that the

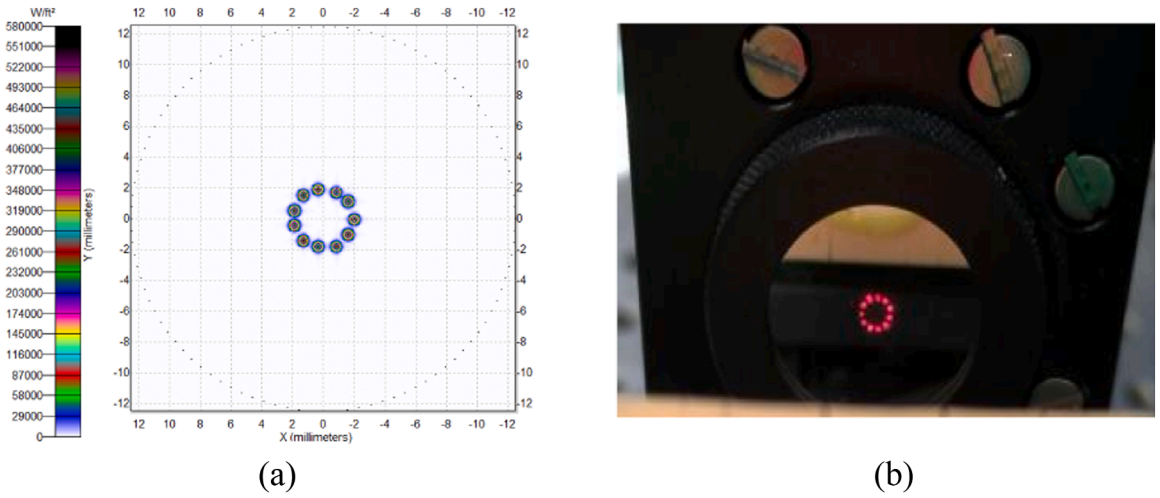

Fig. 4. Schematic diagram of the simulated spot distribution on the surface of the spherical mirror (a). Actual observed light spot distribution map (b).

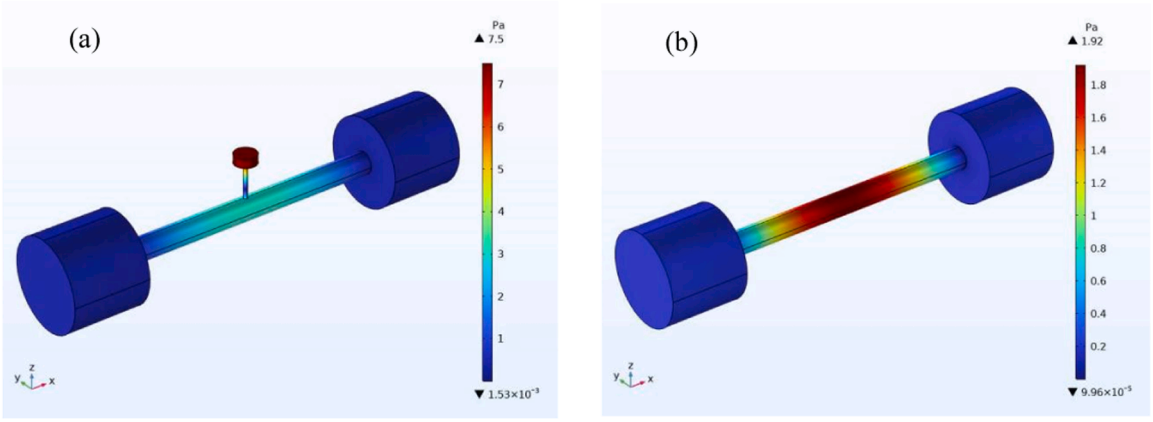

Fig. 5. The acoustic pressure distribution of MVCA-PAC (a) and traditional resonant PA cell (b).

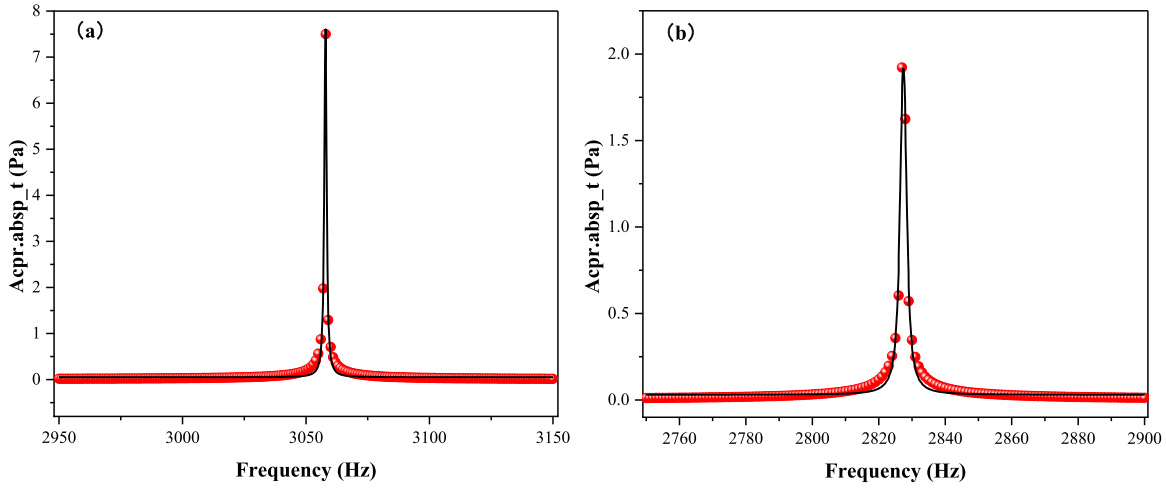

Fig. 6. The simulated acoustic pressure amplitude-frequency response curve of the MVCA-PAC(a) and traditional resonant PA cell (b).

modulation frequency of the light source matches the resonance frequency of the PA cell, the frequency response characteristics of the designed PAS sensor were experimentally investigated under atmospheric conditions and room temperature. A 1000 ppmv CH_4/N_2 gas mixture was injected into the MVCA-PAC. By varying the modulation frequency of the light source from 1000 Hz to 2000 Hz, the corresponding PAS signal amplitudes are recorded and presented in Fig. 8. A Lorentzian line shape was used to analyze the data, revealing an optimal modulation frequency of 1460 Hz. Therefore, the resonance frequency of the designed PA cell was calculated to be 2920 Hz.

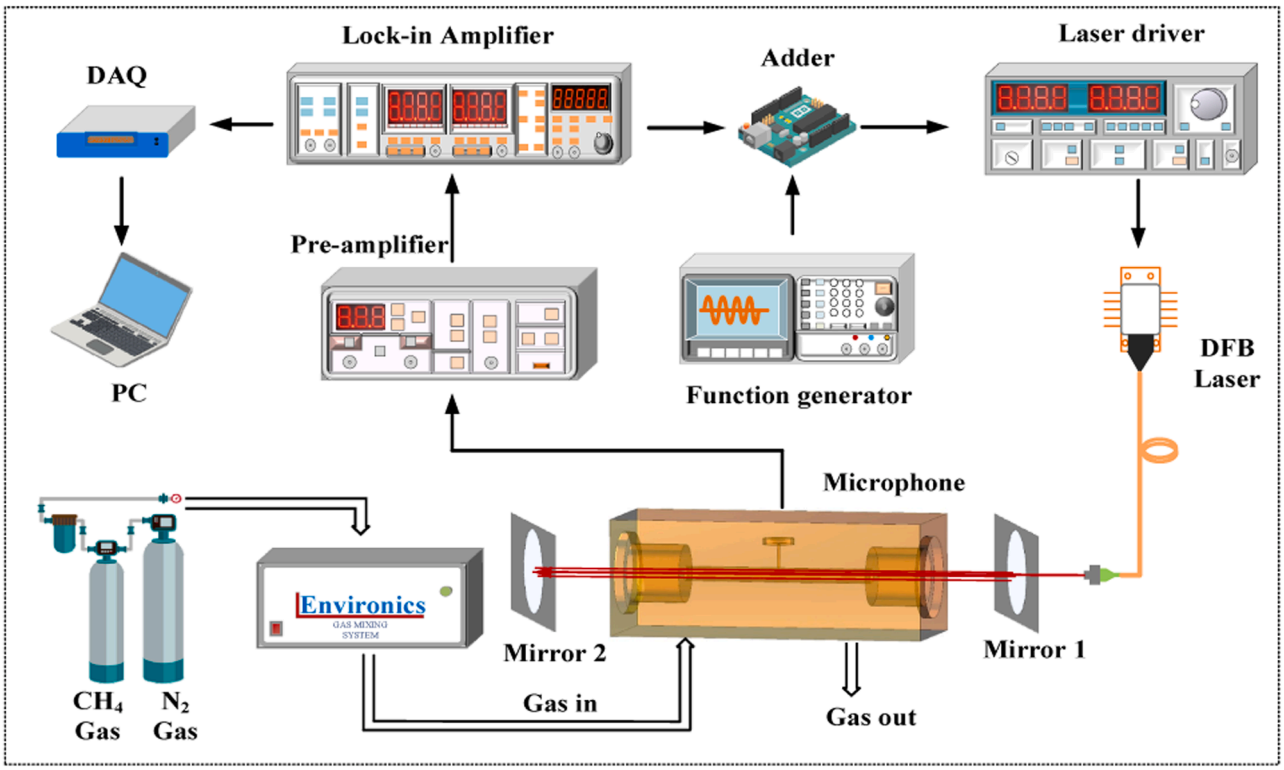

Fig. 7. Schematic diagram of the designed PAS sensor setup based on MVCA-PAC.

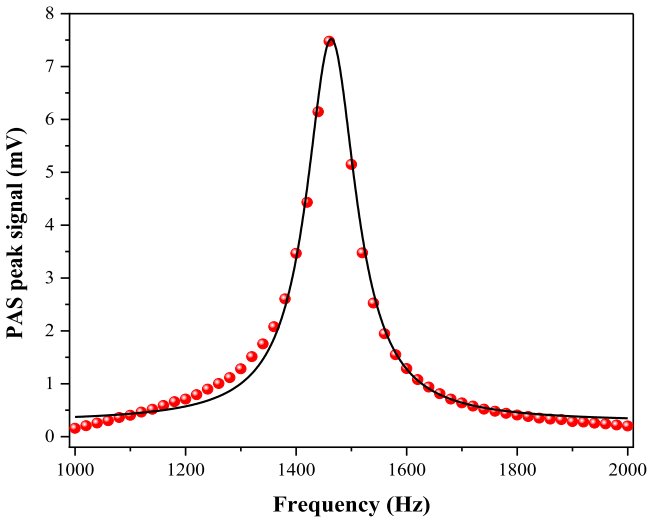

Fig. 8. Frequency response of the PAS sensor based on MVCA-PAC.

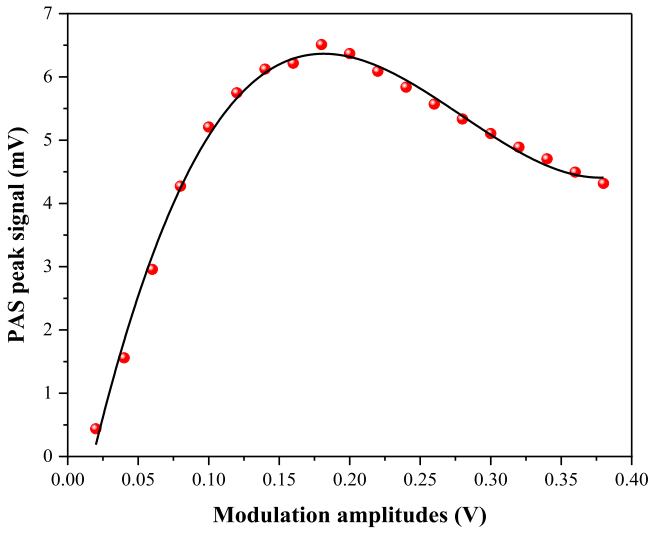

Fig. 9. PAS signal amplitudes as a function of modulation depth.

In addition to the modulation frequency, the PAS signal intensity depends on the modulation depth as well. The optimal modulation depth for CH_4 detection was identified by analyzing the relationship between PAS signal amplitude and modulation depth at the specified modulation frequency. Fig. 9 illustrates the dependence of PAS signal amplitude on modulation depth for 1000 ppm CH_4 gas, the results indicate that the optimal modulation depth for CH_4 detection is 0.18 V.

4.2. *Comparison with traditional resonant PA cell and single-pass cell*

To evaluate the performance of the PAS sensor based on the MVCA-PAC, a traditional resonant PA cell of the same size was used as a replacement for the MVCA-PAC. Both the traditional resonant PA cell and the MVCA-PAC operated under identical multi-reflection optical path conditions. A 1000 ppmv CH_4 gas was transferred into the traditional resonant PA cell and the MVCA-PAC, respectively, with both PAS sensors operate under normal pressure and ambient temperature conditions. The measured 2-*f* signals for the traditional resonant PA cell and the MVCA-PAC are shown in Fig. 10. The peak amplitudes of the PAS signals were 4.66 mv for the traditional resonant PA cell and 9.75 mv for the MVCA-PAC, representing a significant enhancement. This improvement is attributed to the fact that the T-shaped acoustic waveguide effectively collects the acoustic field energy and reduces the acoustic field disturbance and resistance during sound wave propagation, thereby minimizing energy dissipation and facilitating more efficient acoustic wave transmission.

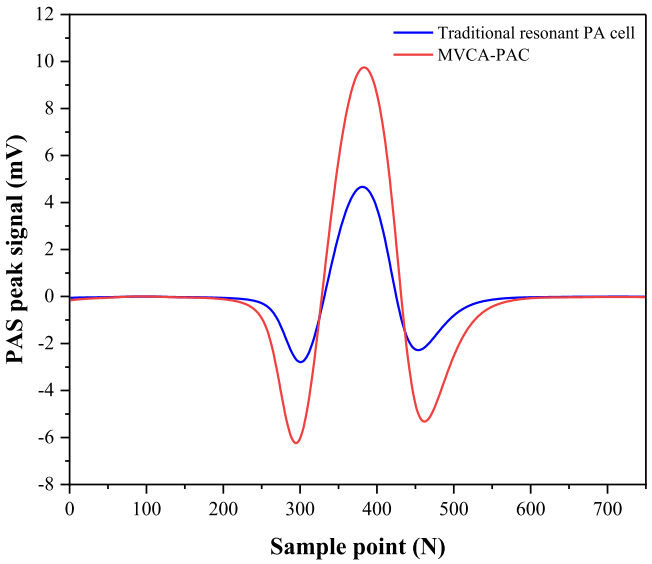

Fig. 10. The measured 2-*f* signals for the traditional resonant PA cell and the MVCA-PAC under the same absorption optical path conditions.

To further conform the enhancement effect of the MVCA-PAC on PAS signals, 2-*f* signal measurements were conducted under both multi-pass and single-pass conditions, as shown in Fig. 11. The results clearly indicate that the signal amplitude of the multi-pass PA cell is substantially higher than that of the single-pass cell. The amplification factor for the multi-pass PA cell was calculated to be approximately 4.5, highlighting the substantial improvement in signal intensity achieved with the multi-pass design.

4.3. Linear response characteristic

The concentration response of the designed PAS sensor was evaluated using CH_4/N_2 gas mixtures with concentrations ranging from 2 ppm to 100 ppm. The gas mixtures were precisely prepared using the Environics Series 4000 gas distribution system and were subsequently introduced into the MVCA-PAC for detailed analysis. The variation of averaged 2-*f* signal amplitudes with CH_4 concentration is illustrated in Fig. 12. The results confirmed an outstanding linear relationship between the PAS sensor response and CH_4 concentration, with an R^2value of 0.999 indicating a highly accurate linear fit.

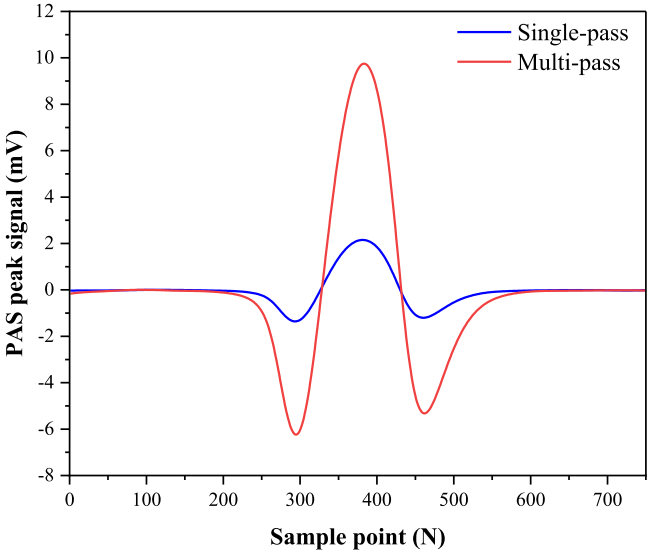

Fig. 11. The measured 2-*f* signals of the MVCA-PAC under multi-pass and single-pass conditions.

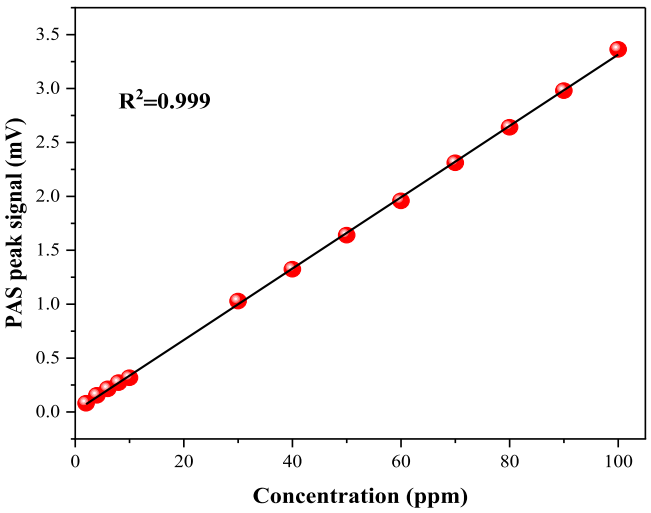

Fig. 12. The measured 2-*f* signal amplitudes as a function of CH_4 concentration.

4.4. MDL of the sensor

The long-term stability and MDL of the PAS sensor based on the MVCA-PAC were evaluated using Allan Variance analysis. The MVCA-PAC was filled with CH_4 gas at a concentration of 60 ppm, and the measurements were conducted over a duration of 2 hours. For the convenience of Allan variance analysis, here the sampling interval of the CH_4 gas PAS signal is 1 s, and no averaging is performed. Fig. 13 shows the Allan Variance as a function of averaging time. The results indicates that the Allan Variance decreases as the averaging time increases. When the averaging time is 300 s, the MDL was calculated to be 0.572 ppm.

4.5. Performance of the algorithm

To evaluate the effect of the CRFOF algorithm in enhancing the measurement precision of the PAS sensor, we performed continuous one-hour measurements of CH_4 at a concentration of 100 ppm. Fig. 14 compares the CH_4 concentration data before and after applying the

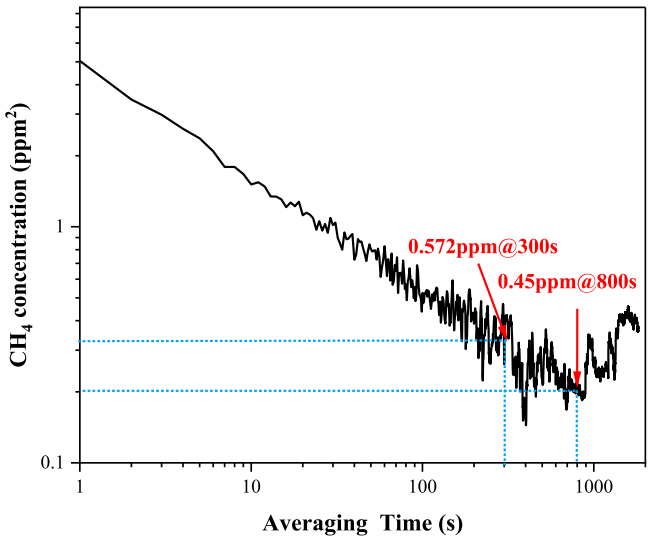

Fig. 13. Allan variance as a function of the averaging time for the PAS sensor based on the MVCA-PAC.

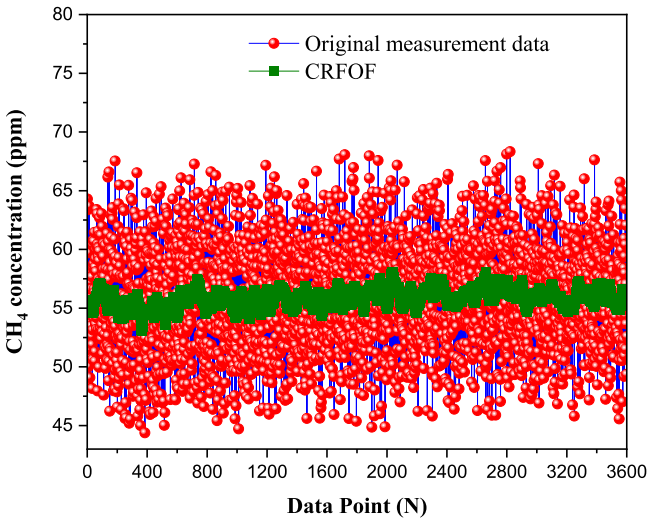

Fig. 14. Methane concentration fluctuations over time before and after processing with the CRFOF algorithm.

CRFOF algorithm, revealing a significant reduction in measurement fluctuations from 23.9 ppm to 5.07 ppm. This result highlights the algorithm's effectiveness in stabilizing concentration readings and improving the system's overall precision. Fig. 15 presents histograms of the continuous CH_4 concentration measurements before and after processing with the CRFOF algorithm. A Gaussian fit was applied to each dataset, with the full width at half maximum (FWHM) of the Gaussian distribution used as a metric to evaluate measurement precision. This approach effectively accounts for the influence of signal fluctuations and noise on the system's performance. The FWHM values of the Gaussian fitting curves for the methane concentration measurements were 8.884 ppm and 0.578 ppm before and after applying the CRFOF algorithm, respectively. These results demonstrate that the CRFOF algorithm enhances the measurement precision of the PAS sensor by a factor of 15.4.

4.6. Online monitoring of CH_4 in the atmospheric

The designed PAS sensor based on MVCA-PAC was deployed in the Laser Intelligent Perception Laboratory at Anqing Normal University, China. Continuous online monitoring of atmospheric CH_4 was conducted over 48 hours from April 12–14, 2024. Outdoor atmospheric samples were continuously pumped into the MVCA-PAC using a sampling pump, and CH_4 concentration measurements was performed in real-time. A filter was installed at the air inlet to prevent interference from impurities and particles. The CH_4 concentration measurements over a continuous 48-hour period, recorded with an averaging time of 300 s, are shown in Fig. 16. The fluctuations in atmospheric methane concentrations may be primarily due to changes in temperature and humidity during the day-night transition, which can potentially affect the absorption efficiency of modulated light by methane molecules. The monitoring data revealed that the average atmosphere methane concentration over the 48-hour period was approximately 1.73 ppm.

5. Conclusion

In this study, we proposed and developed a highly sensitive and compact PAS sensor based on a MVCA-PAC for trace CH_4 gas detection. The sensor system was constructed using a high-power DFB laser, precisely tuned to the CH_4 absorption line near 1653 nm, and its feasibility was successfully demonstrated through experimental validation. By extending the absorption optical path through multiple reflections and employing a T-shaped acoustic waveguide for secondary amplification of the PAS signal, the system achieved significant enhancement in detection performance. The MDL of the sensor was determined to be 0.572 ppm with an averaging time of 300 s, as calculated from Allan variance analysis. The response curves of the designed PAS sensor to different concentrations of CH_4 show an excellent linear correlation between the concentration and the PAS signal, with an R^2 value of

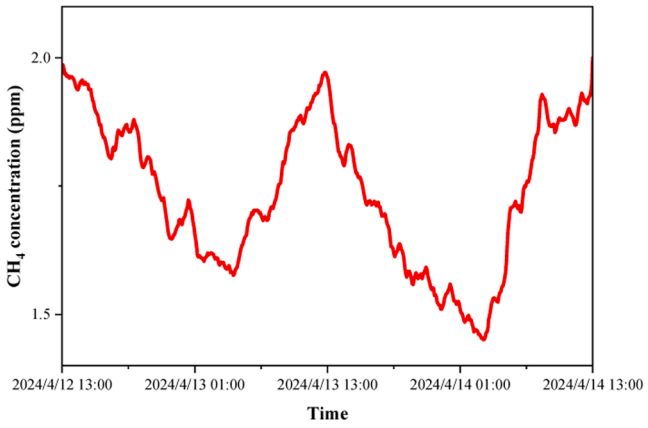

Fig. 16. The measurement CH_4 concentrations in the atmosphere over 48 consecutive hours.

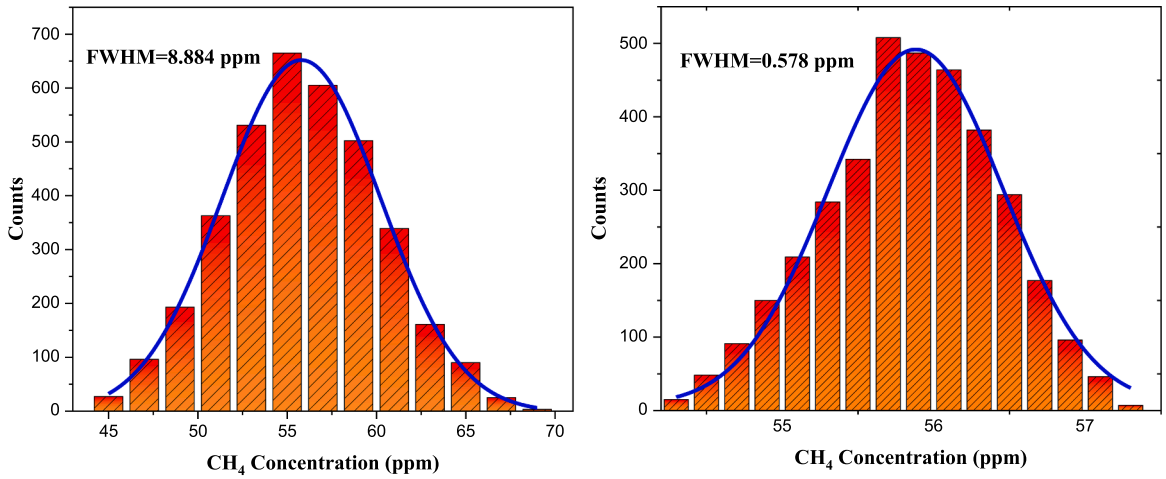

Fig. 15. Statistical histograms of the CH_4 concentration measurements before and after processing with the CRFOF algorithm.

0.999. Additionally, the Chebyshev rational fractional-order filtering algorithm was initially utilized in processing PAS signals. The experimental results demonstrated that the algorithm improved the measurement precision of CH_4 from 8.884 ppm to 0.578 ppm, representing a 15.4-fold enhancement. The sensor was further employed for the continuous, real-time online monitoring of atmospheric CH_4 concentration over a 48-hour period. The results indicated that the system is capable of meetting the requirements for long-term monitoring of atmospheric methane concentrations. The proposed PAS sensor combines high sensitivity, compact design, and robust performance, providing a promising technical solution for the detection of trace CH_4 gas in various applications.

CRediT authorship contribution statement

Cao Yanan: Methodology. **Cheng Gang:** Software. **Zhan Shengbao:** Methodology. **Liu Chen:** Investigation. **Chen Hang:** Investigation. **Zha Shenlong:** Writing – original draft, Investigation. **Pan Pan:** Writing – review & editing. **Li Lingli:** Formal analysis. **Zhang Qilei:** Data curation. **Ma Hongliang:** Methodology. **Guo Yuxiang:** Software.

Declaration of Competing Interest

The authors declare no conflicts of interest.

Acknowledgments

The authors gratefully acknowledge financial supports from the National Natural Science Foundation of China (Grant No. 62205005 and 62105005), Excellent Youth Scientific Research Project in Anhui Province's Universities (Grant No.2023AH030074), Anhui Province Excellent Young Teacher Cultivation Project (Grant No.YQZD2023055), Anhui Province University Research Project (Grant No.2024AH051112 and 2023AH051194) , Key Research and Development Program of Shanxi Province of China (Grant No.202302150101006).

Data availability

Data will be made available on request.

References

[1] E. Nisbet, E. Dlugokencky, P. Bousquet, Methane on the rise—again, Science 343 (2014) 493–495.
[2] T. Strahl, J. Herbst, E. Maier, S. Rademacher, C. Weber, H.-F. Pernau, A. Lambrecht, J. Wöllenstein, Comparison of laser-based photoacoustic and optical detection of methane, J. Sens. Sens. Syst. 10 (2021) 25–35.
[3] K. Liu, L. Wang, T. Tan, G. Wang, W. Zhang, W. Chen, X. Gao, Highly sensitive detection of methane by near-infrared laser absorption spectroscopy using a compact dense-pattern multipass cell, Sens. Actuat. B-Chem. 220 (2015) 1000–1005.
[4] M. Müller, S. Weigl, J. Müller-Williams, M. Lindauer, T. Rück, S. Jobst, R. Bierl, F. Matysik, Comparison of photoacoustic spectroscopy and cavity ring-down spectroscopy for ambient methane monitoring at Hohenpeißenberg, Atmos. Meas. Tech. 16 (2023) 4263–4270.
[5] R. Wang, S. Qiao, Y. He, Y. Ma, Highly sensitive laser spectroscopy sensing based on a novel four-prong quartz tuning fork, Opto-Electron. Adv. 8 (2025) 240275.
[6] Z. Li, J. Chen, L. Li, J. Zhang, J. Yao, Exceptional-point-enhanced sensing in an all-fiber bending sensor, Opto-Electron. Adv. 6 (2023) 230019.
[7] J. Fan, Z. Ou, Z. Zhang, Entangled photons enabled ultrafast stimulated Raman spectroscopy for molecular dynamics, Light Sci. Appl. 13 (2024) 163.
[8] Y. He, Y. Wang, S. Qiao, X. Duan, H. Qi, Y. Ma, Hydrogen-enhanced light-induced thermoelastic spectroscopy sensing, Photonics Res 13 (2025) 194–200.
[9] H. Hu, T. Flöry, V. Stummer, A. Pugzlys, M. Zeiler, X. Xie, A. Zheltikov, A. Baltuska, Hyper spectral resolution stimulated Raman spectroscopy with amplified fs pulse bursts, Light Sci. Appl. 13 (2024) 61.
[10] Y. Ma, S. Qiao, R. Wang, Y. He, C. Fang, T. Liang, A novel tapered quartz tuning fork-based laser spectroscopy sensing, Appl. Phys. Rev. 11 (2024) 041412.
[11] J. Jing, K. Liu, J.F. Jiang, T.H. Xu, S. Wang, T. Liu, Highly sensitive and stable probe refractometer based on configurable plasmonic resonance with nano-modified fiber core, Opto-Electron. Adv. 6 (2023) 220072.
[12] C. Zhang, S. Qiao, Y. He, C. Liu, Y. Ma, Multi-resonator T-type photoacoustic cell based photoacoustic spectroscopy gas sensor for simultaneous measurement C_2H_2, CH_4 and CO, Sens. Actuators B-Chem. 427 (2025) 137168.
[13] H. Sun, Y. He, S. Qiao, Y. Liu, Y. Ma, Highly sensitive and real-simultaneous CH_4/C_2H_2 dual-gas LITES sensor based on Lissajous pattern multi-pass cell, Opto-Electron. Sci. 3 (2024) 240013.
[14] L. Shi, Y. Li, Z. Li, Early cancer detection by SERS spectroscopy and machine learning, Light Sci. Appl. 12 (2023) 234.
[15] Z. Lang, S. Qiao, Y. Ma, Fabry–Perot-based phase demodulation of heterodyne light-induced thermoelastic spectroscopy, Light Adv. Manuf. 4 (2023) 23.
[16] Y. Ma, T. Liang, S. Qiao, X. Liu, Z. Lang, Highly sensitive and fast hydrogen detection based on light-induced thermoelastic spectroscopy, Ultra Sci. 3 (2023) 0024.
[17] Y. Wang, J. Zhang, Y. Zheng, Y. Xu, J. Xu, J. Jiao, Y. Su, H. Lu, K. Liang, Brillouin scattering spectrum for liquid detection and applications in oceanography, Opto-Electron. Adv. 6 (2023) 220016.
[18] Q. Yu, Z. Yao, J. Zhou, W. Yu, C. Zhuang, Y. Qi, H. Xiong, Transient stimulated Raman scattering spectroscopy and imaging, Light Sci. Appl. 13 (2024) 70.
[19] X. Wang, X. Qiu, M. Liu, F. Liu, M. Li, L. Xue, B. Chen, M. Zhang, P. Xie, Flat soliton microcomb source, Opto-Electron. Sci. 2 (2023) 230024.
[20] S. Dong, D. He, Q. Zhang, C. Huang, Z. Hu, C. Zhang, L. Nie, K. Wang, W. Luo, J. Yu, B. Tian, W. Wu, X. Chen, F. Wang, J. Hu, X. Xiao, Early cancer detection by serum biomolecular fingerprinting spectroscopy with machine learning, eLight 3 (2023) 17.
[21] K. Hashimoto, T. Nakamura, T. Kageyama, V.R. Badarla, H. Shimada, R. Horisaki, T. Ideguchi, Upconversion time-stretch infrared spectroscopy, Light Sci. Appl. 12 (2023) 48.
[22] A. Li, Y. Wu, C. Wang, F. Bao, Z. Yang, S. Pan, An inversely designed integrated spectrometer with reconfigurable performance and ultra-low power consumption, Opto-Electron. Adv. 7 (2024) 240099.
[23] Z. Lang, S. Qiao, Y. He, Y. Ma, Disturbance-immune, fast response LITES gas sensor based on out-plane vibration mode employing micro Fabry-Perot cavity with heterodyne phase demodulation, Sens. Actuat. B-Chem. 419 (2024) 136412.
[24] M. Shao, C. Ji, J. Tan, B. Du, X. Zhao, J. Yu, B. Man, K. Xu, C. Zhang, Z. Li, Ferroelectrically modulate the Fermi level of graphene oxide to enhance SERS response, Opto-Electron. Adv. 6 (2023) 230094.
[25] H. Ma, Y. Chen, S. Qiao, Y. He, Y. Ma, A high sensitive methane QEPAS sensor based on self-designed trapezoidal-head quartz tuning fork and high power diode laser, Photoacoustics 42 (2025) 100683.
[26] C. Zhang, Y. He, S. Qiao, Y. Liu, Y. Ma, High-sensitivity trace gas detection based on differential Helmholtz photoacoustic cell with dense spot pattern, Photoacoustics 38 (2024) 100634.
[27] Y. Ma, Y. Liu, Y. He, S. Qiao, H. Sun, Design of multipass cell with dense spot patterns and its performance in a light-induced thermoelastic spectroscopy-based methane sensor, Light Adv. Manuf. 6 (2025) 1.
[28] Q. Yang, Y. Hu, V. Torres-Company, K. Vahala, Efficient microresonator frequency combs, eLight 4 (2024) 18.
[29] Y. Liu, S. Qiao, C. Fang, Y. He, H. Sun, J. Liu, Y. Ma, A highly sensitive LITES sensor based on a multi-pass cell with dense spot pattern and a novel quartz tuning fork with low frequency, Opto-Electron. Adv. 7 (2024) 230230.
[30] T. Minamikawa, R. Sakaguchi, Y. Harada, H. Tanioka, S. Inoue, H. Hase, Y. Mori, T. Takamatsu, Y. Yamasaki, Y. Morimoto, M. Kawasaki, M. Kawasaki, Long-range enhancement for fluorescence and Raman spectroscopy using Ag nanoislands protected with column-structured silica overlayer, Light Sci. Appl. 13 (2024) 299.
[31] H. Sun, S. Qiao, Y. He, Y. Liu, Y. Ma, Highly sensitive CH_4, C_2H_2 and CO simultaneous measurement LITES sensor based on multi-pass cell with overlapped spots pattern and novel QTFs with low resonant frequency, Opt. Express 32 (2024) 28183–28194.
[32] B. Fu, R. Gao, N. Yao, H. Zhang, C. Li, J. Lin, M. Wang, L. Qiao, Y. Cheng, Soliton microcomb generation by cavity polygon modes, Opto-Electron. Adv. 7 (2024) 240061.
[33] J. Panger, E. Moser, M. Müller, S. Weigl, S. Jobst, T. Rück, R. Bierl, F.-M. Matysik, A sub-ppbv-level acetone and ethanol quantum cascade laser based photoacoustic sensor—characterization and multi-component spectra recording in synthetic breath, Photoacoustics 30 (2023) 100473.
[34] Q. Wei, B. Li, B. Zhao, P. Yang, EC-QCL based photoacoustic spectroscopy for detection of SF_6 decomposition components, Sens. Actuat. B-Chem. 369 (2022) 132351.
[35] I. Sherstov, D. Kolker, V. Vasiliev, A. Pavlyuk, M. Miroshnichenko, A. Boyko, N. Kostyukova, I. Miroshnichenko, Laser photo-acoustic methane sensor (7.7 μm) for use on unmanned aerial vehicles, Infrared Phys. Technol. 133 (2023) 104865.
[36] S. Li, Y. Yuan, Z. Shang, X. Yin, A. Sampaolo, P. Patimisco, V. Spagnolo, L. Dong, H. Wu, Ppb-level NH_3 photoacoustic sensor combining a hammer-shaped tuning fork and a 9.55 μm quantum cascade laser, Photoacoustics 33 (2023) 100557.
[37] J. Panger, M. Müller, T. Rück, S. Weigl, R. Bierl, Characterizing a sensitive compact mid-infrared photoacoustic sensor for methane, ethane and acetylene detection considering changing ambient parameters and bulk composition (N_2, O_2 and H_2O), Sens. Actuat. B-Chem. 352 (2022) 130962.
[38] T. Seoudi, J. Charensol, W. Trzpil, F. Pages, D. Ayache, R. Rousseau, A. Vicet, M. Bahriz, Highly sensitive capacitive MEMS for photoacoustic gas trace detection, Sensors 23 (2023) 3280.
[39] K. Liu, Y. Cao, G. Wang, W. Zhang, W. Chen, X. Gao, A novel photoacoustic spectroscopy gas sensor using a low cost polyvinylidene fluoride film, Sens. Actuators B-Chem. 277 (2018) 571–575.

[40] Z. Lang, S. Qiao, Y. Ma, Acoustic microresonator based in-plane quartz-enhanced photoacoustic spectroscopy sensor with a line interaction mode, Opt. Lett. 47 (2022) 1295–1298.
[41] C. Zhang, S. Qiao, Y. He, S. Zhou, L. Qi, Y. Ma, Differential quartz-enhanced photoacoustic spectroscopy, Appl. Phys. Lett. 122 (2023) 241103.
[42] Z. Shang, H. Wu, G. Wang, S. Li, L. Dong, Theoretical analysis and experimental optimization of an elliptical acoustic resonator in quartz-enhanced photoacoustic spectroscopy, Sens. Actuators B-Chem. 373 (2022) 132718.
[43] A. Zifarelli, M. Giglio, G. Menduni, A. Sampaolo, P. Patimisco, V. Passaro, H. Wu, L. Dong, V. Spagnolo, Partial least-squares regression as a tool to retrieve gas concentrations in mixtures detected using quartz-enhanced photoacoustic spectroscopy, Anal. Chem. 92 (2020) 11035–11043.
[44] Y. Ma, Y. He, Y. Tong, X. Yu, F.K. Tittel, Quartz-tuning-fork enhanced photothermal spectroscopy for ultra-high sensitive trace gas detection, Opt. Express 26 (2018) 32103–32110.
[45] S. Qiao, Y. He, H. Sun, P. Patimisco, A. Sampaolo, V. Spagnolo, Y. Ma, Ultra-highly sensitive dual gases detection based on photoacoustic spectroscopy by exploiting a long-wave, high-power, wide-tunable, single-longitudinal-mode solid-state laser, Light Sci. Appl. 13 (2024) 100.
[46] C. Fang, T. Liang, S. Qiao, Y. He, Z. Shen, Y. Ma, Quartz-enhanced photoacoustic spectroscopy sensing using trapezoidal-and round-head quartz tuning forks, Opt. Lett. 49 (2024) 770–773.
[47] A. Sampaolo, P. Patimisco, M. Giglio, A. Zifarelli, H. Wu, L. Dong, V. Spagnolo, Quartz-enhanced photoacoustic spectroscopy for multi-gas detection: A review, Anal. Chim. Acta 1202 (2022) 338894.
[48] H. Yi, O. Laurent, S. Schilt, M. Ramonet, X. Gao, L. Dong, W. Chen, Simultaneous monitoring of atmospheric CH_4, N_2O, and H_2O using a single gas sensor based on Mid-IR quartz-enhanced photoacoustic spectroscopy, Anal. Chem. 94 (2022) 17522–17532.
[49] C. Li, Y. Zhang, M. Guo, H. Qi, X. Zhao, K. Chen, Differential cantilever enhanced fiber-optic photoacoustic sensor for diffusion gas detection, Anal. Chem. 96 (2024) 4562–4569.
[50] J. Karhu, M. Nyman, S.-K. M, T. Hieta, Cantilever-enhanced photoacoustic measurement of HTO in water vapor, Photoacoustics 29 (2023) 100443.
[51] T. Strahl, J. Steinebrunner, C. Weber, J. Wöllenstein, K. Schmitt, Photoacoustic methane detection inside a MEMS microphone, Photoacoustics 29 (2023) 100428.
[52] Y. Ma, Y. Hong, S. Qiao, Z. Lang, X. Liu, H-shaped acoustic micro-resonator-based quartz-enhanced photoacoustic spectroscopy, Opt. Lett. 47 (2022) 601–604.
[53] K. Chen, B. Zhang, S. Liu, F. Jin, M. Guo, Y. Chen, Q. Yu, Highly sensitive photoacoustic gas sensor based on multiple reflections on the cell wall, Sens. Actuators A: Phys. 290 (2019) 119–124.
[54] K. Krzempek, A. Hudzikowski, A. Głuszek, G. Dudzik, K. Abramski, G. Wysocki, M. Nikodem, Multi-pass cell-assisted photoacoustic/photothermal spectroscopy of gases using quantum cascade laser excitation and heterodyne interferometric signal detection, Appl. Phys. B 124 (2018) 1–6.
[55] Y. Ma, S. Qiao, Y. He, Y. Li, Z. Zhang, X. Yu, F.K. Tittel, Highly sensitive acetylene detection based on multi-pass retro-reflection-cavity-enhanced photoacoustic spectroscopy and a fiber amplified diode laser, Opt. Express 27 (2019) 14163–14172.
[56] M. Zhang, B. Zhang, K. Chen, M. Guo, S. Liu, Y. Chen, Z. Gong, Q. Yu, Z. Chen, M. Liao, Miniaturized multi-pass cell based photoacoustic gas sensor for parts-per-billion level acetylene detection, Sens. Actuators A: Phys. 308 (2020) 112013.
[57] X. Du, Q. Zhang, Y. Wei, T. Zhang, Y. Zhang, Y. Li, Research on denoising of second harmonic signal in photoacoustic spectroscopy based on SSA-VMD-WTD method, Infrared Phys. Technol. 138 (2024) 105204.

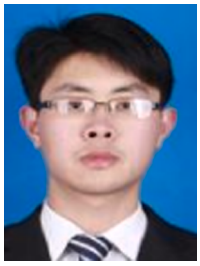

Shenlong Zha received his PhD degree in optics from the University of Science and Technology of China in 2017. Currently, he is an associate Professor at Anqing Normal University, China. His research interests include optical sensors, trace gas detection, photoacoustic spectroscopy and its applications.

Hang Chen is currently pursuing a master's degree of information and communication engineering from Anqing Normal University, China. Her research interests include optical sensors and quartz enhanced photoacoustic spectroscopy.

Chen Liu is currently pursuing a master's degree of information and communication engineering from Anqing Normal University, China. His research interests include optical sensors and photoacoustic spectroscopy.

Yuxiang Guo is an associate professor at Anqing Normal University, China. He received his PhD degree in control theory and engineering from the Beijing University of Aeronautics and Astronautics, in 2017. His research interests include optical signal processing, advanced control theory and application.

Hongliang Ma is an associate professor at Anqing Normal University, China. He received his PhD degree in optics from the University of the Chinese Academy of Sciences, in 2016. His research interests include atmospheric molecular infrared absorption spectroscopy, mid-infrared difference frequency generation sources, and trace gas concentration detection.

Qilei Zhang is a lecturer in School of Electronic Engineering and Intelligent Manufacturing at Anqing Normal University, China. He received his PhD degree in optics from the University of the Chinese Academy of Sciences, in 2018. His research interests include spectral analysis, reaction mechanism of VOCs.

Lingli Li is a lecturer in School of Electronic Engineering and Intelligent Manufacturing at Anqing Normal University, China. She got her Ph.D. degree in optics from University of Chinese Academy of Sciences in 2014. Her research interests include super-resolution optical imaging, micro/nano optics, and micro-nano manufacturing technology.

Shengbao Zhan is a professor in School of Electronic Engineering and Intelligent Manufacturing at Anqing Normal University, China. He received his Ph. D degree in optical communication from Air Force Engineering University in 2008. His research interests include fiber laser, optical communications, and spectral beam combining of fiber lasers

Gang Cheng is an associate professor at Anhui University of Technology. He received his Ph.D. degree from the University of Science and Technology of China in 2019. His research interests are absorption spectroscopy and photoacoustic spectroscopy.

Yanan Cao is an associate professor at Anhui University of Technology. He received his Ph.D. degree in optics from the University of Science and Technology of China in 2018. His current research interests include optical design and simulation and laser spectroscopy.

Pan Pan is a professor in School of Electronic Engineering and Intelligent Manufacturing at Anqing Normal University, China. She got her Ph. D. degree in physical electronics from Institute of Semiconductors, Chinese Academy of Sciences in 2015. Her research interests include photonic integrated devices and their applications in communication and gas detection.